Seventh International Conference on Computational Fluid Dynamics (ICCFD7), Big Island, Hawaii, July 9-13 2012

ICCFD7–3205

A Two-Dimensional Model of Blood Plasma Flow with Oxygen Transport and Blood Cell Membrane Deformation

Y. Tekleab*, W. Harris*,**
Corresponding author: ytekleab@mit.edu

* Research Assistant – Department of Aeronautics and Astronautics
Massachusetts Institute of Technology, Cambridge, MA, USA
* Professor of Aeronautics and Astronautics, Associate Provost for Faculty Equity
Massachusetts Institute of Technology, Cambridge, MA, USA

Abstract: Sickle cell disease (SCD) is a genetic disorder that alters the red blood cell (RBC) structure and function such that hemoglobin (Hb) cannot effectively bind and release oxygen. Our novel 2-D computational model represents a fast, time efficient method developed to analyze flow dynamics, O_2 diffusion, and cell deformation in the microcirculation. A finite difference, Crank-Nicholson scheme is used to compute the flow and O_2 concentration, and the level set computational method is used to advect the RBC membrane on a staggered grid. Simulation data implicates a few parameters to be significant in the perturbation of the blood flow and O_2 concentration profiles.

Keywords: microcirculation, sickle cell, red blood cell, finite difference, level set, Crank-Nicholson, blood flow, oxygen diffusion.

1 Introduction

The need for a systemic macroscopic model of human blood flow in the capillaries is driven by the desire to improve the state of knowledge of the impact of several diseases on various human organs. The diseases include leukemia, malaria, and sickle cell anemia. A systemic macroscopic model of human blood flow in the capillaries simultaneously accounts for the blood plasma dynamics, blood cell deformation and convection, oxygen diffusion across the blood cell membrane, and transport of oxygen into the blood plasma and tissue of the surrounding capillaries. In the case of sickle cell disease, which is a genetic disorder that alters the red blood cell structure and function such that hemoglobin cannot effectively bind and release oxygen, the physical modeling requires proper consideration for severe red blood cell membrane deformation. Assuming the blood plasma to be incompressible and the flow to be constant temperature, a systemic macroscopic model of human blood flow in the capillaries consists of the conservation of mass, Navier-Stokes equation, diffusion equation, blood cell membrane geometry, and appropriate boundary and initial conditions. Le Floch [1] has developed and implemented an unsteady, three-dimensional systemic macroscopic model of human blood flow in the capillaries showing agreement with existing experimental results. In this paper we develop and implement an unsteady, two-dimensional model and compare its results with existing experimental and simulated results.

2 Problem Statement

We aim to develop a simplified two-dimensional model of the microcirculation that accounts for plasma and RBC flow, oxygen diffusion from the red cell into the surrounding tissue, and the evolving shape and membrane stresses on the red cell. In order to accurately model both the sickle and healthy microcirculation, we begin by creating a simplified physical model of our system. In the human body, blood vessels contain several different types of cells, proteins, antigens, and molecules, although the vast majority of the blood is comprised of plasma and RBCs. The capillaries are the smallest of blood vessels and are formed by endothelial cells, with a thickness of only one cell. The capillaries form a vast network throughout the body, allowing the delivery of oxygen to all tissue. Immediately surrounding the vessel wall, there is a very thin interstitial space that may contain interstitial fluid.

Accounting for all of these objects within the blood and regions in the microcirculation can become costly in a computational model. Due to the relatively high fraction of RBCs and plasma in the blood, and the thin regions of vascular walls and interstitial space, we choose to neglect these regions [2]. Based on the regions included, a 3-layer model of the physical system is developed (shown in Figure 1) as a basis for our computational domain.

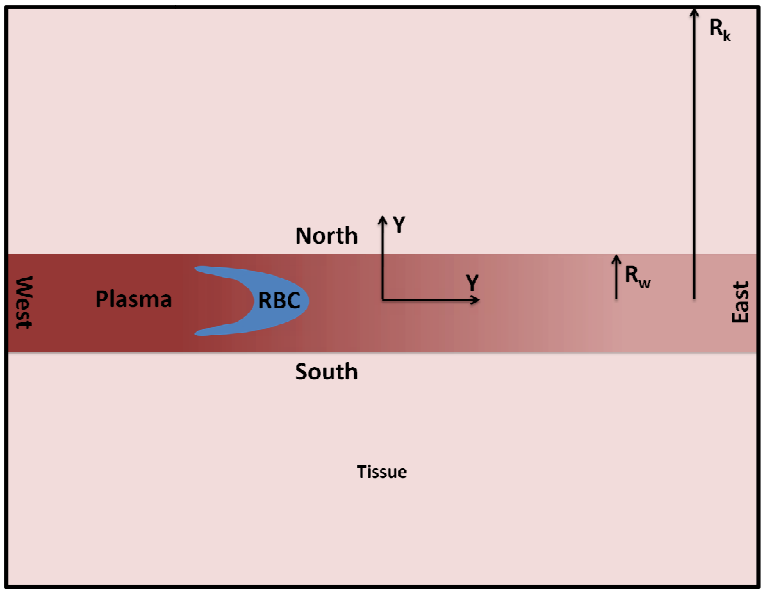

Figure 1 – Computational domain in 3-Layer Model

Coordinate axes at the center of the computational domain

Next, we approach the characterization of the physical system described above. The microcirculation plasma flow and oxygen transport are modeled by the following set of governing equations for our system:

(1) Mass continuity equation
(2) Incompressible Navier-Stokes equation
(3) Fick's Law of mass diffusion

$$\nabla \cdot \underline{v} = 0 \ , \tag{1}$$

$$\rho\left(\frac{\partial \underline{v}}{\partial t} + \underline{v} \cdot \nabla \underline{v}\right) = -\nabla p + \mu \nabla^2 \underline{v} \ , \tag{2}$$

$$\frac{\partial c}{\partial t} + \nabla \cdot \left(c\underline{v} - D_{ox}\nabla c\right) = R(c) \ , \tag{3}$$

The physical 3-layer model is then transformed onto a grid, and the governing equations are translated into the computational model

3 Computational Model

The computational model for the capillary flow was constructed using Matlab® software. The blood plasma flow and oxygen concentration calculations are solved using a finite difference method on a static, staggered, Marker-and-Cell (MAC) grid. The finite difference scheme used to solve the blood plasma flow conditions is based on a Navier-Stokes solver developed by Benjamin Seibold of the Mathematics Department at MIT. [3]

Table 1 – Plasma Flow Parameters

Parameter	Value
ρ	$1025\ \frac{kg}{m^3}$
V_{avg}	$10^{-3}\ \frac{m}{s}$
D_{cap}	$8\times10^{-6}\,m$
μ	$1.5\times10^{-3}\,Pa\cdot s$
$Re = \frac{\rho V_{avg} D_{cap}}{\mu}$	5.47×10^{-3}

The plasma and RBC membrane interactions are implemented using the level set method. [4]

A Cartesian coordinate system is used because the physical system is approximated as a 2D plasma flow on a rectangular surface, as shown in Figure 1. The RBC is modeled as an elastic membrane with a bending stiffness k_{RBC}. The properties of the blood flow are listed in Table 1.

3.1 Blood Plasma Flow

The compactness and efficiency of Seibold's method results from the fixed geometry and static discritization of the grid. This allows for the system matrices to be the same at each time step and therefore need to be computed only once. [3]

The blood plasma follows the 2D incompressible Navier-Stokes equations, (2) and (3), and is constrained by the incompressible 2D mass continuity, equation (1). The dimensionless, scalar component versions of these equations are shown below.

$$u_x + v_y = 0 \ , \tag{4}$$

$$u_t = -(u^2)_x - (uv)_y + \frac{1}{Re}\left(u_{xx} + u_{yy}\right) - p_x \ , \tag{5}$$

$$v_t = -(uv)_x - (v^2)_y + \frac{1}{Re}\left(v_{xx} + v_{yy}\right) - p_y \ , \tag{6}$$

The time step updates for velocity components U^n and V^n will be computed in a series of steps, by incorporating each term in the Navier-Stokes equations. First, we will incorporate the nonlinear advective terms from equation (5), $\left[-(u^2)_x - (uv)_y\right]$, and equation (6), $\left[-(uv)_x - (v^2)_y\right]$. The first updated values of velocity will be denoted as U^* and V^*. These values are solved explicitly using an upwinding scheme as shown in equations (7) and (8).

$$\frac{U^* - U^n}{\Delta t} = -((U^n)^2)_x - (U^n V^n)_y \ , \tag{7}$$

$$\frac{V^* - V^n}{\Delta t} = -(U^n V^n)_x - ((V^n)^2)_y \ , \tag{8}$$

Next we update velocity by incorporating the viscosity terms, $\left[\frac{1}{Re}\left(u_{xx} + u_{yy}\right)\right]$ and $\left[\frac{1}{Re}\left(v_{xx} + v_{yy}\right)\right]$, implicitly.

$$\frac{U^{**} - U^*}{\Delta t} = \frac{1}{Re}\left(U^{**}_{xx} + U^{**}_{yy}\right) \ , \tag{9}$$

$$\frac{V^{**} - V^*}{\Delta t} = \frac{1}{Re}\left(V^{**}_{xx} + V^{**}_{yy}\right) \ , \tag{10}$$

Finally, we can update the velocity by including the pressure terms, $[-p_x]$ and $\left[-p_y\right]$, implicitly.

$$\frac{U^{n+1} - U^{**}}{\Delta t} = -(P^{n+1})_x \ , \tag{11}$$

$$\frac{V^{n+1} - V^{**}}{\Delta t} = -(P^{n+1})_y \ , \tag{12}$$

Equations (11) and (12) can be rewritten in vector form as,

$$\frac{\underline{U}^{n+1} - \underline{U}^{**}}{\Delta t} = -\nabla P^{n+1} \ , \tag{13}$$

The pressure is found by computing the divergence of both sides, which eliminates the $\underline{U}^{n+1}$ term due to the continuity constraint, and you are left with

$$-\frac{\nabla \cdot \underline{U}^{**}}{\Delta t} = -\Delta P^{n+1} \ , \tag{14}$$

Applying the inverse Laplacian operator to equation (14) then gives the pressure at the new time step (P^{n+1}). Finally, we can take the gradient of the pressure field to obtain the velocities.

$$\underline{G}^{n+1} = -\nabla \mathrm{P}^{\mathrm{n+1}} \ , \tag{15}$$

$$\underline{U}^{n+1} = \underline{U}^{**} + \Delta t \underline{G}^{n+1} \ , \tag{16}$$

As mentioned previously, the efficiency of these calculations is in large part due to having calculated the system matrices only once before marching through the finite difference scheme. The system matrices for our system are essentially inverse Laplacian operators. These system matrices are implemented using the Crank-Nicolson scheme, which is second-order accurate in time and space.

Spatial and Time Discritization

The advection term calculation above uses a centered difference scheme, which is second order accurate as opposed to a forward or backward difference scheme. Despite the higher order of accuracy, using a centered difference scheme can create oscillations due to the coupling of the variables because they are all calculated at the same points. To eliminate this phenomenon, we use a staggered grid. [3]

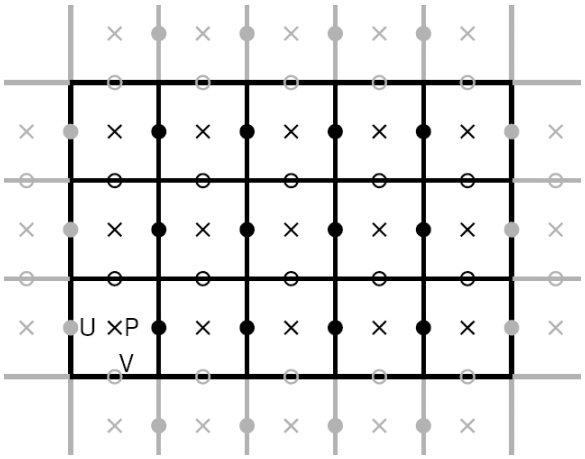

Figure 2 – Staggered MAC Grid

Interior cells are shown in black and boundary cells are shown in gray. Crosses denote cell centers where fluid pressure and other quantities are calculated. The circles denote the cell borders where velocity components are calculated (U-velocity in filled circles and V-velocity in unfilled circles)

Consider a rectangular domain, which is discretized into rectangular elements on a staggered grid. In this grid, the velocities are defined on the boundaries and the pressures are defined in the centers of the cell as shown in Figure 2.

For our solution to converge with stability, we must satisfy the Courant–Friedrichs–Lewy (CFL) condition. The limiting time step will be for the explicit upwind calculation of the advection terms. The diffusion terms are calculated using a second-order accurate, Crank-Nicolson scheme, which is unconditionally stable [5]. Therefore, to ensure overall stability, the following conditions must hold true.

CFL condition for advective term:

$$u_{max}\frac{\Delta t}{\Delta x} + v_{max}\frac{\Delta t}{\Delta x} \leq 1 \ , \tag{17}$$

The horizontal and vertical grid sizes are the same; $\Delta x = \Delta y = h$, therefore,

$$(u_{max} + v_{max})\frac{\Delta t}{h} \leq 1 \ , \tag{18}$$

$$\Delta t \leq \frac{h}{(u_{max} + v_{max})} \ , \tag{19}$$

We desire a time step as large as possible to reduce computational time for the simulation, but small enough to ensure stability. Equation (19) shows that the maximum time step is related to the grid spacing and maximum speed of the flow within the capillary, which changes in time. Instead of choosing a new time step at each iteration, we can choose a time step small enough such that it always satisfy the CFL condition.

Since we are using non-dimensional equations for our model, all quantities are relative and the actual values are meaningless before they are dimensionalized. By design, we can set the initial velocity at all points within the flow to unity, and the maximum velocity should not exceed this value by much more. Test cases of the model with very small time steps have shown that the maximum velocity does not exceed three. For total certainty, we will use the value of four for the maximum velocity.

Next, we must calculate the grid size. All of our equations have been non-dimensionalized using the capillary diameter as a reference length. Therefore the diameter of the capillary will be set to unity and all other values will be proportional. The length of our channel will be set to be a multiple of the diameter.

Based on computational time and accuracy, the optimal grid step size is determined to be $h = 0.02$. Using equation (19) and the values determined for grid step size and maximum velocity, the time step is calculated, $\Delta t = 0.0050$. Test simulations however, show much smoother results for a lower time step of $\Delta t = 0.0025$, therefore we will be using this value.

For our flow calculations, it is important that we can calculate velocities, pressures, and their derivatives at the same points.

We can find these values at neighboring locations by averaging or by finding first or second differences for the derivatives.

Flow Boundaries

The flow is bounded by two other regions. The first, on the north and south boundaries, is the capillary wall. At the capillary wall, the plasma velocity is zero because we impose a no slip / no flux condition. The east and west border of the computational domain are set to be periodic. The flow velocities and pressure gradient are also periodic such that the flow properties are continuous on the east and west boundaries of the capillary channel.

$$\underline{v}_N = \underline{v}_S = 0 \ , \tag{20}$$

$$\underline{v}_E = \underline{v}_W \ , \tag{21}$$

The second boundary is the RBC membrane. The flow properties for this boundary and inside the RBC will be discussed in the next section.

3.2 RBC Membrane

The level set method is used to dictate the advection of the RBC membrane. A function $\phi(x, y)$ is produced in the mesh space such that $\phi(x, y) = 0$ defines the boundary between the cell and the plasma. The domain inside the boundary, Ω^-, is defined by $\phi(x, y) < 0$, and the domain outside the boundary, Ω^+, is defined by $\phi(x, y) > 0$. Our zero level set function is initially approximated as an ellipse with the semi-major axis along the diameter of the capillary and the semi-minor axis along the axis of the capillary.

The rate at which the level set function propagates depends on the flow speed. This propagation will follow the convection equation:

$$\phi_t + \underline{v} \cdot \nabla\phi = 0 \ , \tag{22}$$

By definition, the gradient of the level set function is parallel to the velocity vector. Therefore, we can rewrite our velocity vector as the product of the magnitude of the velocity, F, and unit vector in the direction of the level set function, $\frac{\nabla\phi}{|\nabla\phi|}$. Substituting these quantities into equation (22) yields the level set function.

$$\phi_t + F|\nabla\phi| = 0 \ , \tag{23}$$

In order to determine F, the propagation rate, we can use the dot product of the velocity and gradient of the level set:

$$\underline{v} \cdot \nabla\phi = F\hat{n} \cdot \nabla\phi \ , \tag{24}$$

$$\langle u, v\rangle \cdot \langle \phi_x, \phi_y\rangle = F\frac{\nabla\phi}{|\nabla\phi|}\cdot\nabla\phi \ , \tag{25}$$

$$u\phi_x + v\phi_y = F|\nabla\phi| \ , \tag{26}$$

$$u\phi_x + v\phi_y = F\frac{\phi_x^2 + \phi_y^2}{\sqrt{\phi_x^2 + \phi_y^2}} \ , \tag{27}$$

$$F = \frac{u\phi_x + v\phi_y}{\sqrt{\phi_x^2 + \phi_y^2}} \ , \tag{28}$$

The propagation rate, F, is calculated at each iteration, and as shown in equation (28), F is dependent on the plasma flow velocity. For greater accuracy, the level set function is moved onto a finer mesh and propagated on this grid at a proportionally smaller time step. It is then returned to the original, coarser mesh. This allows us to have a more accurate advection scheme while saving time by running the rest of the simulation at such a coarser mesh.

The fluid both inside and outside the RBC are governed by the Navier-Stokes equations, however, the RBC membrane acts on the fluid as an additional body force. Unlike the capillary wall, the RBC membrane does not have a no-slip condition. In our computational model, the flow is discontinuous at the boundary due to the reactionary body force of the membrane acting on the cytoplasm. These membrane stresses on the fluid can be expressed as a jump in pressure across the fluid; therefore, they can be incorporated into the Navier-Stokes calculations of the plasma flow. This pressure jump must be accounted for when calculating the pressure of a fluid element that accesses a pressure of a neighboring cell that is on the opposite side of the membrane.

Figure 3 illustrates an example of a point (i, j) which has two points in its stencil on the opposite side of the level set boundary. The stencil for the 2nd difference of the pressure would be written as

$$\begin{aligned}\frac{1}{(h_x)^2}\left(p_{i-1,j} - 2p_{i,j} + p_{i+1,j}\right) + \frac{1}{\left(h_y\right)^2}\left(p_{i-1,j} - 2p_{i,j} + p_{i+1,j}\right) \\ = f_{i,j} + \frac{a_R}{(h_x)^2} + \frac{a_T}{\left(h_y\right)^2} \ ,\end{aligned} \tag{29}$$

The a_R and a_T terms account for the pressure jump, across the boundary for the right-hand $(i+1, j)$ and top $(i, j+1)$ points respectively, caused by the stress applied on the fluid by the RBC membrane. Notice that there are no additional terms for the left-hand $(i-1, j)$ or bottom $(i, j-1)$ points because they are on the same side of the boundary as the center point (i, j) of the stencil.

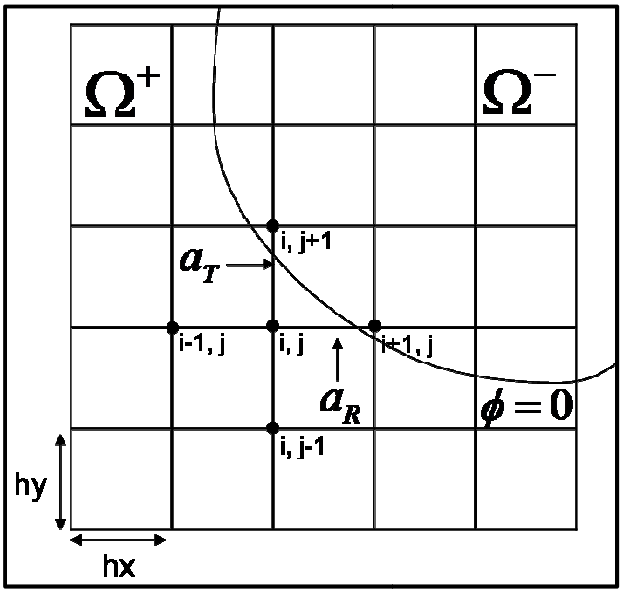

Figure 3 – Jump condition at RBC boundary

Jump conditions $\boldsymbol{a_T}$ and $\boldsymbol{a_R}$ are shown on a 5-point stencil. Jump conditions are applied for points on the stencil that lie in a different domain than the center point.

RBC membrane stiffness is a uniform value across the membrane, but varies for healthy and sickle erythrocytes. We use a value of $k_{RBC} = 1.9 \times 10^{-5} \frac{N}{m}$ for healthy erythrocytes [6]. In sickle erythrocytes, the membrane stiffness is dependent on local oxygen concentration.

As the oxygen diffuses out of the cell, the oxyhemoglobin complexes are unbound, producing free oxygen and consequently, change their molecular conformation, leaving them vulnerable to polymerization in the sickle case. Although my model does not directly simulate the polymerization of HbS and its affect on the RBC shape, this model does capture the increase in cell membrane rigidity for the sickle RBC.

Berger and King propose an inverse exponential relationship between stiffness and oxygen concentration.

$$\frac{k_{RBC}}{(k_{RBC})_0} = \left(\frac{c}{c_0}\right)^{-j} = \left(\frac{p_{O_2}}{(p_{O_2})_0}\right)^{-j}, \tag{30}$$

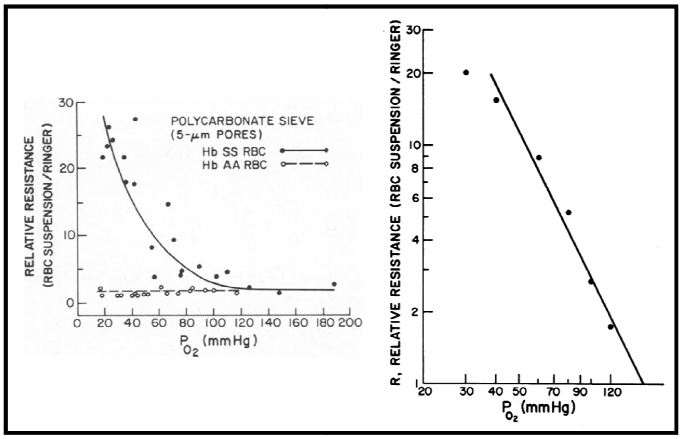

Figure 4 – RBC Membrane Stiffness vs. O_2 Partial Pressure [7]

Membrane stiffness for healthy and sickle RBCs plotted on linear and log-log plots. The plots indicate an exponential relationship between membrane stiffness and O_2 partial pressure for sickle RBCs, and no change in membrane stiffness for healthy RBCs.

In equation (30), $(k_{RBC})_0$ represents the stiffness of a normal cell; c_0 and $(p_{O_2})_0$ represent the oxygen concentration and oxygen partial pressure when the cell is fully oxygenated at the arterial end of the capillary. The stiffness index, j, is a positive constant. Berger and King use experimental data to justify the stiffness index value.

Figure 4 shows the non-dimensional resistance, which we refer to as $\frac{k_{RBC}}{(k_{RBC})_0}$, plotted against the oxygen partial pressure in both linear and log-log axes. Based on these plots, it appears that a stiffness index of $j = 2$ is reasonable. Based on the slope from the best-fit line on the logarithmic plot, it appears that a stiffness index of $j = 2$ is reasonable value.

This value, however, serves as an upper bound for the stiffness index because in the experiment, the sickle blood was "allowed sufficient time to equilibrate with the oxygen tension" [8]. Therefore, the stiffness index will vary in the range $0 \leq j \leq 2$.

The membrane stress is calculated as the product of the membrane stiffness and the curvature of the membrane.

$$\sigma = k_{RBC}\kappa \ , \tag{31}$$

where the curvature, κ, is calculated from the level set function,

$$\kappa = \frac{\phi_{xx}\phi_y^2 - 2\phi_x\phi_y\phi_{xy} + \phi_{yy}\phi_x^2}{\left(\phi_x^2 + \phi_y^2\right)^{\frac{3}{2}}} \ , \tag{32}$$

This is also a simplification in the model. Creating a stress function that is directly proportional to curvature assumes that at rest, the membrane would take the shape of a circle, the shape that would minimize overall stress on the object. However in reality, at rest, the RBC has a bi-concave shape. As the fluid within and exterior to the cell moves, it will deform the RBC, causing different stress levels on the cell membrane.

This could have some impact on the results of this simulation, by creating the appearance of higher stress values at the points of greatest curvature. Additionally, this model might slightly decrease the apparent surface area of the RBC, which could impact the velocity profiles. This would not impact the oxygen diffusion however, because the diffusion calculations are dependent on the volume of the RBC, not the surface area, which is controlled to remain unchanging with each time step.

The membrane stress at each grid point adjacent to the membrane is calculated to account for the total pressure jump. These values are summed into a matrix, J, which is added to the pressure term when P^{n+1} is calculated.

3.3 Oxygen Diffusion

The oxygen diffusion is incorporated into our computational model, allowing us to observe the oxygen concentration throughout the system as the RBC traverses the capillary. The oxygen diffusion component must model the oxygen-hemoglobin interaction, oxygen diffusion throughout the RBC, plasma, and tissue, the oxygen-myoglobin interaction (binding of free oxygen), and the consumption of free oxygen.

Like the fluid pressure, the oxygen concentration will be calculated at the cell centers in our computational grid. Therefore, all saturation values, flow velocities, and oxygen concentration derivatives must be averaged or differenced to provide values at the cell centers as well. Simplifying equation (3) by applying 2D Cartesian coordinates, and the constraint of continuity, we obtain equation (33) in the computational domain.

$$\frac{C^{n+1}-C^n}{\Delta t}+U^nC_x^n+V^nC_x^n-D_{ox}\left(C_{xx}^n+C_{yy}^n\right)=R(C^n)\ , \tag{33}$$

The first spatial derivative of the oxygen concentration is calculated using an explicit centered difference scheme. The second spatial derivatives are derived using an implicit Crank-Nicolson scheme. The oxygen concentration update can then be calculated as,

$$C^{n+1}=C^n+\Delta t\left[R(C^n)-U^nC_x^n-V^nC_y^n+D_{ox}\left(C_{xx}^n+C_{yy}^n\right)\right]\ , \tag{34}$$

S^{Hb} and S^{Mb} updates are calculated in a similar fashion. In the computational domain, these equations are written as,

$$\begin{aligned}\frac{S^{Hb^{n+1}}-S^{Hb^n}}{\Delta t}&+U^nS_x^{Hb^n}+V^nS_y^{Hb^n}-D^{Hb}\left(S_{xx}^{Hb^n}+S_{yy}^{Hb^n}\right)\\&=-k_{-1}^{Hb}\left(S^{Hb^n}-\left(1-S^{Hb^n}\right)\left(\frac{C^n}{c_{50\%}^{Hb}}\right)^{\boldsymbol{n}}\right)\ ,\end{aligned} \tag{35}$$

$$\begin{aligned}\frac{S^{Mb^{n+1}}-S^{Mb^n}}{\Delta t}&+U^nS_x^{Mb^n}+V^nS_y^{Mb^n}-D^{Mb}\left(S_{xx}^{Mb^n}+S_{yy}^{Mb^n}\right)\\&=-k_{-1}^{Mb}\left(S^{Mb^n}-\left(1-S^{Mb^n}\right)\left(\frac{C^n}{c_{50\%}^{Mb}}\right)\right)\ ,\end{aligned} \tag{36}$$

R contains no derivatives and is calculated explicitly. In the computational domain, it is written as,

$$\begin{aligned}R^n&=k_{-1}^{Hb}[Hb]\left(S^{Hb^n}-\left(1-S^{Hb^n}\right)\left(\frac{C^n}{c_{50\%}^{Hb}}\right)^{\boldsymbol{n}}\right)\\&+k_{-1}^{Mb}[Mb]\left(S^{Mb^n}-\left(1-S^{Mb^n}\right)\left(\frac{C^n}{c_{50\%}^{Mb}}\right)\right)+M\ ,\end{aligned} \tag{37}$$

Table 2 lists all of the oxygen diffusion constants used in this model for the normal blood and their values in comparison with those of the Le Floch-Harris model. Most parameter values are nearly identical with the exception of the Hill coefficient and the oxygen concentration at 50% hemoglobin and myoglobin saturation.

Table 2 – Oxygen Diffusion Parameters for normal blood

Tekleab-Harris model vs. Le Floch-Harris model

Constant	Symbol	Value	
		Tekleab-Harris Model	**Le Floch-Harris Model**
O_2 diffusion constant	D_{ox}	$2.40\times10^{-9}\frac{m^2}{s}$	$2.41\times10^{-9}\frac{m^2}{s}$
Diffusivity of Hemoglobin	D^{Hb}	$1.40\times10^{-11}\frac{m^2}{s}$	$1.38\times10^{-11}\frac{m^2}{s}$
Diffusivity of Myoglobin	D^{Mb}	$6.10\times10^{-11}\frac{m^2}{s}$	$6.10\times10^{-11}\frac{m^2}{s}$
Hb dissociation rate constant	k_{-1}^{Hb}	$44s^{-1}$	$44s^{-1}$

Mb dissociation rate constant	k_{-1}^{Mb}	$15.6s^{-1}$	N/A
Hb concentration in RBC	$[Hb]$	$21.099\frac{mol}{m^3}$	$21.099\frac{mol}{m^3}$
Mb concentration in tissue	$[Mb]$	$0.4\frac{mol}{m^3}$	$0.4\frac{mol}{m^3}$
O_2 concentration at 50% Hb saturation	$c_{50\%}^{Hb}$	$3.430 \times 10^{-2}\frac{mol}{m^3}$	$4.412 \times 10^{-2}\frac{mol}{m^3}$
O_2 concentration at 50% Mb saturation	$c_{50\%}^{Mb}$	$3.271 \times 10^{-3}\frac{mol}{m^3}$	$7.981 \times 10^{-3}\frac{mol}{m^3}$
O_2 consumption rate in tissue	M	$-6.1321 \times 10^{-3}\frac{mol}{m^3 - s}$	$-6.1321 \times 10^{-3}\frac{mol}{m^3 - s}$
Henry's law constant	α	$1.029 \times 10^{-5}\frac{mol}{m^3 - Pa}$	$1.130 \times 10^{-5}\frac{mol}{m^3 - Pa}$
Hill coefficient [9]	$\boldsymbol{n}$	2.7	2.2

To simulate the sickle blood, we modify four parameters. The diagram in Figure 5 shows the relative values of these four parameters between the normal and sickle cases.

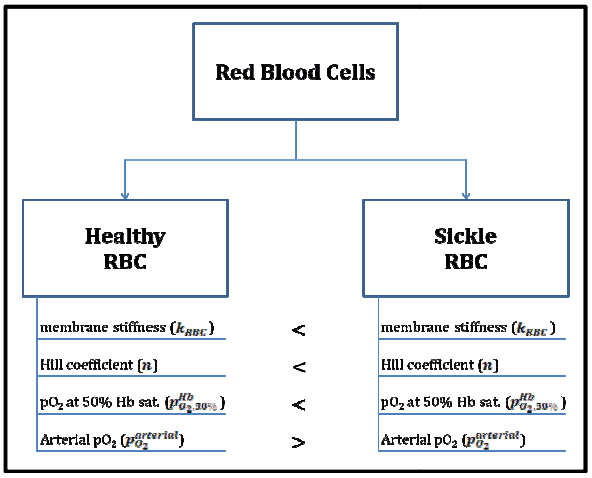

Figure 5 – Healthy vs. Sickle RBC

Notice the increased membrane stiffness, increased pO_2 at 50% Hb saturation, increased Hill coefficient, and decreased arterial pO_2 for the sickle RBC.

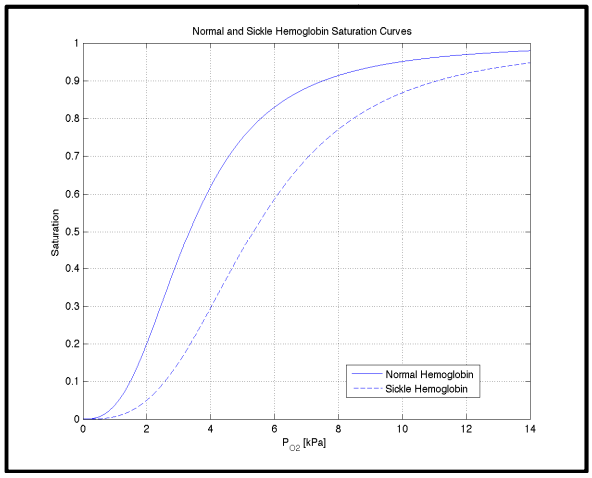

Figure 6 – Normal vs. Sickle Hb Saturation

The increased $\boldsymbol{p_{O_2,50\%}^{Hb}}$, increased Hill coefficient, and decreased $\boldsymbol{p_{O_2}^{arterial}}$ values cause a right-shift in the hemoglobin saturation curve.

The changes in these four parameters in the sickle case cause a right-shift in the hemoglobin oxygen saturation curve.

Figure 6 shows the shifted hemoglobin saturation curve for the sickle case.

4 Conclusion and Future Work

Given specific initial and boundary conditions, the model produced overall results consistent with the basic understanding of flow conditions and oxygen concentration profiles in human capillaries. The simulation data shows several important parameters to be significant in predicting the blood plasma flow, red blood cell membrane deformation, and oxygen concentration profiles.

The perturbations in the oxygen concentration are largely a function of the three sickle parameters, the Hill coefficient ($\boldsymbol{n}$), $p_{O_2,50\%}^{Hb}$, and $p_{O_2}^{arterial}$. The cell membrane stiffness does however, play a small role in the oxygen concentration very close to the RBC. Of the 24 test cases, the first half were simulated with periodic boundary conditions using a smaller computational grid while the second half were simulated with a fixed boundary on the left end and a Neumann boundary condition on the right end. In both sets of test cases, the sickle parameters played the largest role in the oxygen concentration. In the sickle RBC case, the system as a whole has noticeably lower oxygen content than the healthy RBC case. The concentration values are lower in the tissue and the plasma region far from the RBC. This, however, is not the case very close to the RBC. In the plasma region very close to the RBC, and inside the RBC, we observe higher oxygen concentration levels than the healthy case, due to the sickle RBC's poor ability to carry oxygen. The sickle RBC cannot saturate its hemoglobin as much as a healthy RBC due to the right-shift in the saturation curve as shown in Figure 6. Figure 7 illustrates the oxygen diffusion in the microcirculation domain.

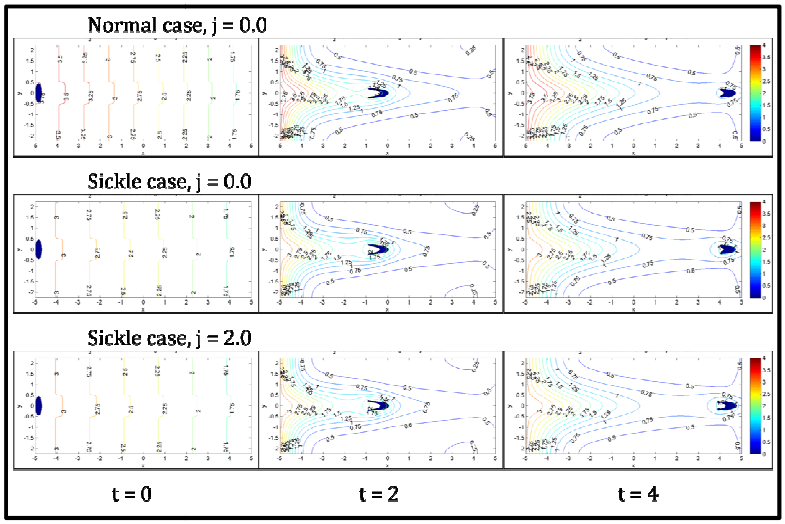

Figure 7 – RBC Deformation and Oxygen Concentration

Figure 8 illustrates the progressive deformation of the RBC and the stress patterns on the RBC membrane. The variable j represents the stiffness index, which varies in the sickle case in the range $0 \leq j \leq 2$. We notice that the stiffness index plays a large role in the membrane stress and shape as well as the rate of membrane deformation.

The Hill coefficient, arterial O_2 partial pressure, O_2 partial pressure at 50% Hb saturation, and cell membrane stiffness are significant factors in the microcirculation oxygen concentration and membrane stress/deformation profiles. The oxygen concentration results were found to be consistent with those of Le Floch [1] and Secomb [10]. Further downstream in the system, the oxygen content of the RBC, the plasma, and the surrounding tissue diminish. Additionally, at any axial cross section in the capillary, the

highest level of oxygen can be found at the center and it diminishes radially such that the tissue furthest away has the lowest concentration.

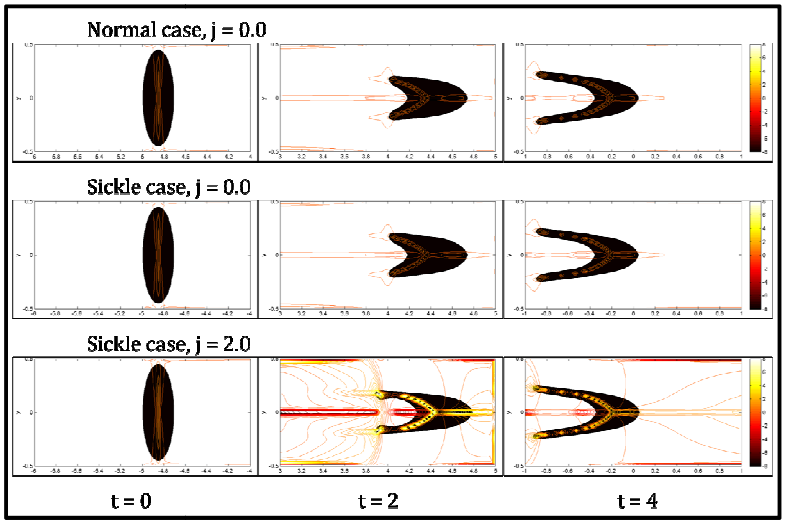

Figure 8 – RBC Deformation and Membrane Stress Profiles

To gain a better understanding of the hemodynamics of the microcirculation using this model, several test cases can be developed for future studies. In these simulations, the flow parameters were unchanged, such as the density and viscosity of plasma, however it may be of interest to investigate whether small changes in these values in both the sickle and healthy cases may impact the perturbations in the flow or the oxygen concentrations. It may also be interesting to create a time-dependent stiffness index such that the membrane stiffness increases with the life of the RBC.

With these improvements to the model, it would be beneficial to see how the data compares to that of other models, such as Le Floch's or Secom's model, allowing for more direct comparisons. It would also be very insightful to compare our data to experimental data conducted either in microfluidic devices or biological samples.

References

[1] F. Le Floch-Yin. *Design of a Numerical Model for Simulation of Blood Microcirculation and Sickle Cell Disease.* (Ph.D. Thesis – Department of Aeronautics and Astronautics). MIT. 2010.

[2] Y. Tekleab. *A Perturbation Model for Normal and Sickle Cell Blood Microcirculation.* (M.S. Thesis – Department of Aeronautics and Astronautics). MIT. 2011.

[3] B. Seibold. *A compact and fast Matlab code solving the incompressible Navier-Stokes equations on rectangular domains*. Applied Mathematics, Massachusetts Institute of Technology. [http://www-math.mit.edu/cse/], 2008.

[4] S. Osher, J. A. Sethian. Fronts propagating with curvature-dependent speed: algorithms based on Hamilton-Jacobi formulations. *Journal of Computational Physics.*, 79: 12-49, 1988.

[5] J. Crank, P. Nicolson. A practical method for numerical evaluation of solutions of partial differential equations of the heat conduction type. *Proc. Camb. Phil. Soc.*, 43 (1): 50–67, 1947.

[6] R. P. Rand, A. C. Burton. Mechanical Properties of the Red Cell Membrane: I. Membrane Stiffness and Intracellular Pressure. *Biophysical J.*, 4(2): 115-135, 1964.

[7] S. Usami, S. Chien, J. F. Bertles. Deformability of Sickle Cells as Studied by Microsieving. *J. Lab. Clin. Med.*, 86: 247-279, 1975.

[8] S. A. Berger, W. S. King. The Flow of Sickle Cell Blood in the Capillaries. *Biophysical J.*, 29(1): 119-148, 1980.

[9] R. M. Winslow. Blood Oxygen Equilibrium Studies in Sickle Cell Anemia. *In Proceedings of the Symposium on Molecular and Cellular Aspects of Sickle Cell Disease.* National Heart, Lung, and Blood Institute, Bethesda, MD. (DHEW Publ. No. (NIH) 76-1007). 235. 1976.

[10] T. Secomb, R. Hsu, A. Pries. Tribology of Capillary Blood Flow. *Proc. IMechE, Part J: Engineering Tribology*, 220:767-774, 2006.